

# Experimental Verification of the 3D Topological Insulator Phase in $\text{PbBi}_2\text{Te}_4$

K. Kuroda,<sup>1</sup> H. Miyahara,<sup>1</sup> M. Ye,<sup>1</sup> S. V. Eremeev,<sup>2,3</sup> Yu. M. Koroteev,<sup>2,3</sup> E. E. Krasovskii,<sup>4,5,6</sup>  
 E. V. Chulkov,<sup>4,5</sup> S. Hiramoto,<sup>1</sup> C. Moriyoshi,<sup>1</sup> Y. Kuroiwa,<sup>1</sup> K. Miyamoto,<sup>7</sup> T. Okuda,<sup>7</sup>  
 M. Arita,<sup>7</sup> K. Shimada,<sup>7</sup> H. Namatame,<sup>7</sup> M. Taniguchi,<sup>1,7</sup> Y. Ueda,<sup>8</sup> and A. Kimura<sup>1,\*</sup>

<sup>1</sup>*Graduate School of Science, Hiroshima University,  
 1-3-1 Kagamiyama, Higashi-Hiroshima 739-8526, Japan*

<sup>2</sup>*Institute of Strength Physics and Materials Science, 634021, Tomsk, Russia*

<sup>3</sup>*Tomsk State University, 634050, Tomsk, Russia*

<sup>4</sup>*Departamento de Física de Materiales UPV/EHU and Centro de  
 Física de Materiales CFM and Centro Mixto CSIC-UPV/EHU,  
 20080 San Sebastián/Donostia, Basque Country, Spain*

<sup>5</sup>*Donostia International Physics Center (DIPC),  
 20018 San Sebastián/Donostia, Basque Country, Spain*

<sup>6</sup>*IKERBASQUE, Basque Foundation for Science, 48011 Bilbao, Spain*

<sup>7</sup>*Hiroshima Synchrotron Radiation Center, Hiroshima University,  
 2-313 Kagamiyama, Higashi-Hiroshima 739-0046, Japan*

<sup>8</sup>*Kure National College of Technology, Agaminami 2-2-11, Kure 737-8506, Japan*  
 (Dated: September 2, 2018)

We show the first experimental evidence of the topological insulator phase in  $\text{PbBi}_2\text{Te}_4$  accompanying a single surface Dirac cone by angle-resolved photoemission spectroscopy (ARPES) with synchrotron radiation. Theoretically it has turned out to have a  $\mathbb{Z}_2$  topological invariant 1; (111). The observed two-dimensional iso-energy contours in the bulk energy gap region are found to be the largest among the other 3D topological insulators established ever. This opens a pathway to realizing the quantum topological transport with a sufficiently large spin current density.

PACS numbers: 73.20.-r, 79.60.-i

Topological insulators recently emerge as a new state of quantum matter, which can be distinguished from conventional insulators. It possesses a massless Dirac fermion in a bulk energy gap whose spin orientations are locked with electron momenta, resulting in a helical spin texture. This newly appeared state of condensed matter can be topologically classified with their characteristic number, so called  $\mathbb{Z}_2$  topological invariants [1, 2]. Generally, the massless Dirac cone can be created at the interface of two materials: topological and ordinary insulators. Such unique properties could provide a fertile ground to realize new phenomena in condensed matter physics, such as a magnetic monopole arising from the topological magneto-electric effect and Majorana fermions hosted superconductor [3, 4]. Owing to time-reversal symmetry, topological surface states are protected from backscattering in the presence of a weak perturbation, which is required for the realization of dissipationless spin transport without external magnetic fields in novel quantum devices [5, 6].

A number of materials that hold spin-polarized surface Dirac cones have been intensively studied, such as  $\text{Bi}_{1-x}\text{Sb}_x$  [7, 8],  $\text{Bi}_2\text{Te}_3$  [9, 10],  $\text{Bi}_2\text{Se}_3$  [11–13, 17], and thallium-based compounds [18–24]. Among them,  $\text{Bi}_2\text{Se}_3$  has been regarded as one of the most promising candidates for potential applications in ultra-low power consumption quantum devices that can work stably at room temperature due to a sufficiently large bulk energy gap. Although significant efforts have been made

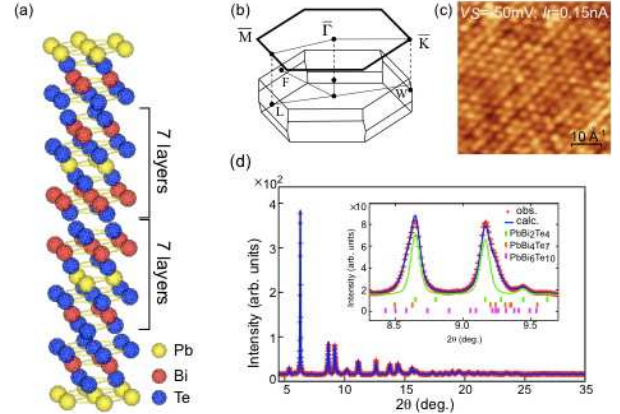


FIG. 1: (color online) (a) Crystal structure  $\text{PbBi}_2\text{Te}_4$ . (b) Bulk and surface Brillouin zones of  $\text{PbBi}_2\text{Te}_4$ . (c) Scanning tunneling microscopy (STM) image acquired at a sample bias ( $V_s$ ) of -50 mV. (d) Measured x-ray powder-diffraction pattern (+) and result of simulation (solid line) using Rietveld technique.

towards spintronic applications using the quantum topological transport, the surface contribution to conduction was hardly observed even at low bulk carrier density [14–16]. This sends us in search of new topological insulators with higher density of spin-polarized Dirac fermions.

Recently, some of the Pb-based ternary chalcogenides have been proposed as the 3D topological insulators [25–27]. The present study is focused on  $\text{PbBi}_2\text{Te}_4$  forming

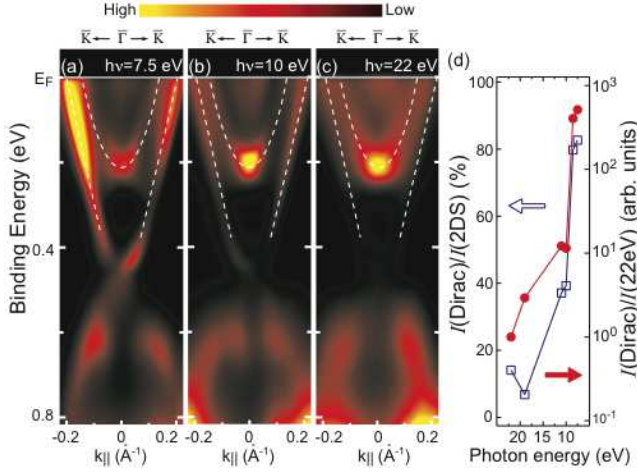


FIG. 2: (color online) (a)-(c) ARPES energy dispersion curves along the  $\bar{\Gamma}$ - $\bar{K}$  line acquired at  $h\nu = 7.5, 10$ , and  $22$  eV, respectively. (d) Integrated photoemission intensity in the binding energy range  $0.3$ - $0.4$  eV of the Dirac cone with respect to parabolic 2D state  $I(\text{Dirac})/I(2\text{DS})$  (open square). Also the corresponding intensity normalized to that taken at  $h\nu = 22$  eV  $I(\text{Dirac})/I(22\text{eV})$  is plotted with filled circles.

the most fundamental structure unit among them, which is composed of seven-layer (7L) blocks formed by the atomic layer sequence Te-Bi-Te-Pb-Te-Bi-Te as shown in Fig.1(a) [28]. The theoretical analysis with an inclusion of spin-orbit coupling indicates that this compound is a three-dimensional topological insulator [27]. In this *Letter*, we show the first experimental evidence of the topological surface state in  $\text{PbBi}_2\text{Te}_4$  by angle-resolved photoemission spectroscopy (ARPES). It has been clarified that the size of two-dimensional iso-energy contours, being proportional to the surface carrier density, is the largest among the other 3D topological insulators established ever. Thus the  $\text{PbBi}_2\text{Te}_4$  can be counted as one of the most promising candidates for realizing quantum topological transport with a large spin current density.

A single crystalline sample of  $\text{PbBi}_2\text{Te}_4$  was grown by the standard procedure using Bridgman method. Stoichiometric mixtures of Pb(5N), Bi(5N) and Te(5N) were melted in evacuated quartz ampoules at  $820^\circ\text{C}$  for a day and then slowly cooled down to  $100^\circ\text{C}$ . The sample quality was checked by high-precision synchrotron radiation powder diffraction experiments using the Large Debye-Scherrer Camera installed at SPring-8 BL02B2. The high-energy incident beam of  $35$  keV (wavelength  $0.35368(3)$   $\text{\AA}$ ) was used to reduce absorption by heavy atoms in the samples. The obtained diffraction pattern is mainly explained for  $\text{PbBi}_2\text{Te}_4$  but the complete fit can be obtained by taking into account other small phases of  $\text{PbBi}_4\text{Te}_7$  and  $\text{PbBi}_6\text{Te}_{10}$  [29–31]. The samples were cleaved along the basal plane and cut into the size of  $1.5 \times 1.5 \times 0.5$   $\text{mm}^3$  for the ARPES measurement. The cleaved surface plane clearly shows an atomi-

cally well-defined order with hexagonal lattice as demonstrated by the scanning tunneling microscope (STM) (Fig.1(c)). Photoemission experiment was performed with synchrotron radiation at the linear undulator beamline (BL1) and the helical undulator beamline (BL9A) of Hiroshima Synchrotron Radiation Center (HiSOR). The ARPES spectra were acquired with a hemispherical photoelectron analyzer (VG-SCIENIA R4000) at  $17$  K. The overall energy and angular resolutions were set at  $10$ - $20$  meV and  $0.3^\circ$ , respectively.

Figures 2(a), 2(b) and 2(c) show the ARPES energy dispersion curves along the  $\bar{\Gamma}$ - $\bar{K}$  line of the surface Brillouin zone (Fig.1(b)) measured at  $h\nu = 7.5, 10$ , and  $22$  eV, respectively. First, we see the parabolic band with the energy minima at the binding energy ( $E_B$ ) of  $200$  meV, exhibiting a strong photoemission intensity near the  $\bar{\Gamma}$  point for all excitation energies. The position of energy minima is unchanged regardless of different incident photon energy as seen in Figs.2(a)-(c), which confirms the two-dimensional nature of this electronic state. More importantly, a linearly dispersive feature, i.e. the Dirac cone with a crossing point at  $E_B = 470$  meV is observed and it is pronounced when excited at  $h\nu = 7.5$  eV, while it is quite weak at  $h\nu = 22$  eV. Note here that the observed spectra are quite homogeneous and reproducible without any indication of contributions from different crystal phases. As the incident photon energy increases, the Dirac cone intensities are suppressed with respect to the parabolic band structure around  $k_{||} = 0$   $\text{\AA}^{-1}$ . The integrated photoemission intensity in the  $E_B$  region of  $300$ - $400$  meV normalized to that taken at  $22$  eV, where only the Dirac cone exists, is plotted as a function of the incident photon energy in Fig.2(d). Note that the Dirac cone was not clearly observed taken up to  $h\nu \sim 50$  eV (not shown). It is apparent that the ratio of spectral weight from the Dirac cone with respect to the parabolic 2D band steeply increases below  $h\nu = 10$  eV. This unusual photon energy dependence could be explained by matrix-element effects in photoemission.

Figures 3(a) and 3(b) summarize the constant energy contours (upper) and their second derivatives (lower) in  $\mathbf{k}$  space ( $-0.3 \text{\AA}^{-1} \leq k_x, k_y \leq +0.3 \text{\AA}^{-1}$ ) from  $0$  meV to  $470$  meV measured from the Dirac point at  $h\nu = 10$  and  $7.5$  eV, respectively. At the Dirac point energy, we find the six ellipses extended along the  $\bar{\Gamma}$ - $\bar{M}$  line in addition to the point-like feature at the  $\bar{\Gamma}$  point for the Dirac state when excited at  $h\nu = 10$  eV. On the other hand, the corresponding elliptical contours are much less visible at  $h\nu = 7.5$  eV, which confirms its bulk state origin. In going away from the Dirac point, the hexagonally shaped contour is solely observed at  $180$  meV and then another state starts to be enclosed inside the Dirac cone at  $210$  meV, suggesting the onset of the bulk conduction band (BCB) because its shape sensitively depends on the incident photon energy, see Figs.3(a) and 3(b). Above  $310$  meV, the Dirac cone is further deformed and is almost merged into

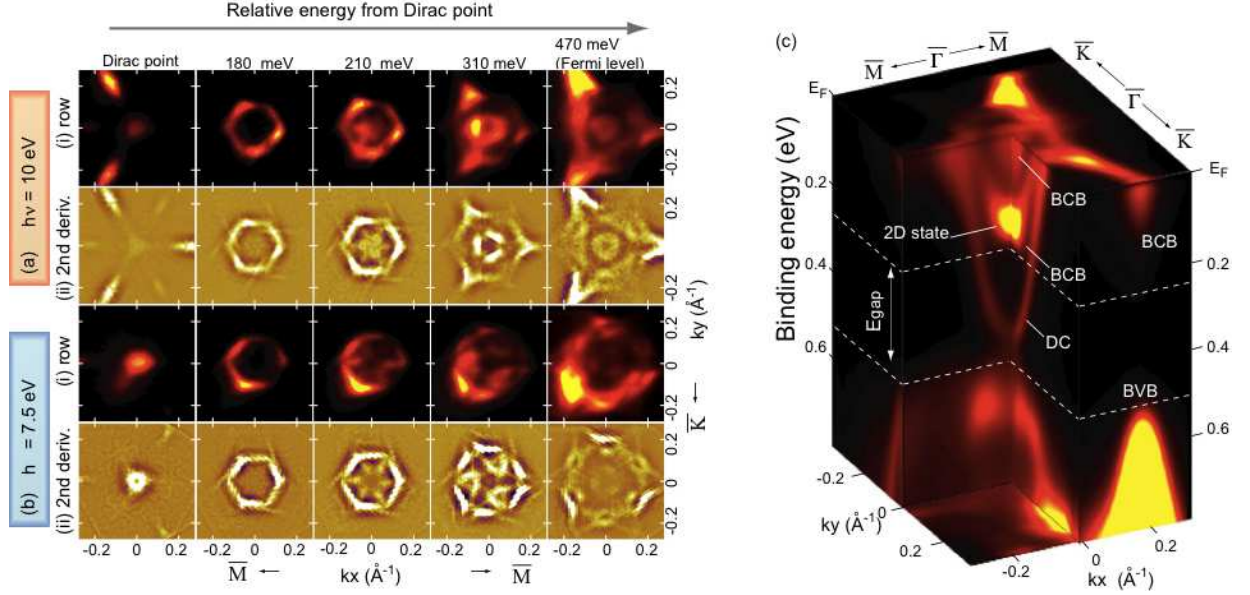


FIG. 3: (color online) Constant energy contour maps (i) and their second derivatives (ii) obtained from the ARPES measurement at  $h\nu=10$  eV (a) and 7.5 eV (b) in  $k$  space ( $-0.3 \text{ \AA}^{-1} \leq k_x, k_y \leq +0.3 \text{ \AA}^{-1}$ ) from 0 meV (Dirac point) to 470 meV (Fermi level). Here the three-fold symmetrization procedure is applied only for the second derivative images. (c) Constructed three dimensional map ( $h\nu=10$  eV).

the bulk conduction band. Additionally, the deformed Fermi surface (FS) of the Dirac cone encloses two large and one small triangular shaped surfaces at  $h\nu=10$  eV surrounding  $\bar{\Gamma}$  point. At  $h\nu=7.5$  eV, the FS enclosing  $\bar{\Gamma}$  point changes their shapes into complicated ones, which also confirms its bulk state origin. The size of the energy gap is estimated as 230 meV as shown in the three dimensional map ( $h\nu=10$  eV) (Fig.3(c)). This large energy gap guarantees the high stability of topological quantum transport at room temperature. We also see the anisotropic valence band features along different symmetry lines. We notice that the valence band maximum is found at  $E_B=490$  meV ( $k_{\parallel}=\pm 0.3 \text{ \AA}^{-1}$ ) for  $\bar{M}-\bar{\Gamma}-\bar{M}$  line, while it is located deeper along  $\bar{K}-\bar{\Gamma}-\bar{K}$  line.

Next we discuss the detailed features of the surface Dirac cone of  $\text{PbBi}_2\text{Te}_4$  by comparing with those of the other 3D topological insulators,  $\text{Bi}_2\text{Se}_3$  and  $\text{TlBiSe}_2$  along  $\bar{\Gamma}-\bar{M}$  and  $\bar{\Gamma}-\bar{K}$  lines as depicted in Fig.4(a). The energy dispersion of  $\text{PbBi}_2\text{Te}_4$  is as steep as those of the other materials near  $E_F$ , but it is apparently less steeper near the Dirac point. The group velocity of this Dirac cone is estimated as  $3.9 \times 10^5$  m/s at  $E_F$ , while, near the Dirac point, it is significantly lower ( $1.4 \times 10^5$  m/s) than those of  $\text{Bi}_2\text{Se}_3$  ( $2.9 \times 10^5$  m/s) [12] and  $\text{TlBiSe}_2$  ( $3.9 \times 10^5$  m/s) [20]. The slower group velocity (less steeper dispersion) would inversely provide an advantage. The sizes of the iso-energy contours in the bulk energy gap region from the Dirac point to 200 meV are much larger for  $\text{PbBi}_2\text{Te}_4$  than corresponding sizes in the other two materials as shown in Fig.4(b). The estimated topological surface carrier density of  $\text{PbBi}_2\text{Te}_4$  obtained from

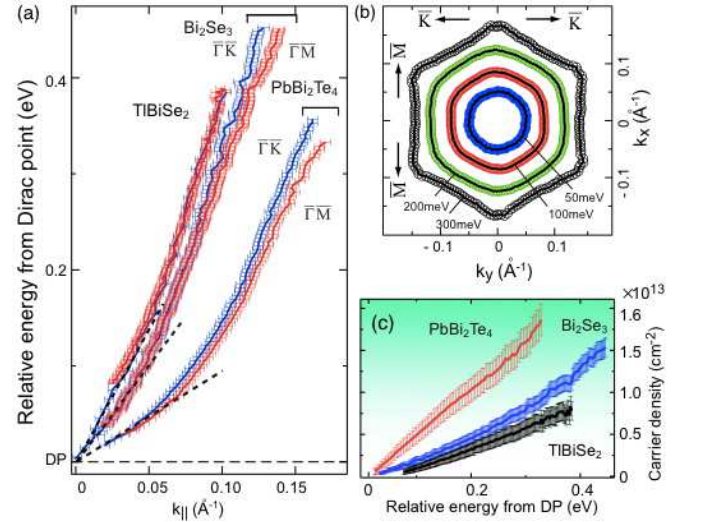


FIG. 4: (color online) (a) Experimental energy dispersion curves of surface Dirac cones for  $\text{PbBi}_2\text{Te}_4$  together with those of  $\text{Bi}_2\text{Se}_3$  and  $\text{TlBiSe}_2$  along  $\bar{\Gamma}-\bar{M}$  and  $\bar{\Gamma}-\bar{K}$  lines obtained from intensity maxima of momentum distribution curves. Here, the energy is measured from Dirac point. (b) Constant energy contours at several energies of obtained after the three-fold symmetrization for  $\text{PbBi}_2\text{Te}_4$ . (c) Estimated carrier densities ( $= S(E)/4\pi^2$ ) for three materials as a function of energy with respect to Dirac point, where  $S(E)$  denotes the area of constant energy contour at energy  $E$ .

the area of constant energy contour  $S(E)/4\pi^2$  is much larger than those of the other two materials (Fig.4(c)).

Figure 5(a) and 5(b) respectively show the theoretic



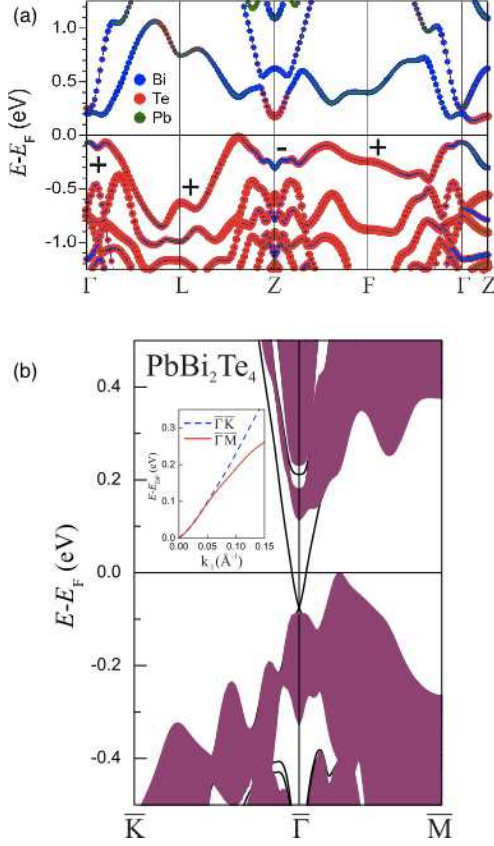


FIG. 5: (color online) (a) Bulk band structure of  $\text{PbBi}_2\text{Te}_4$  calculated along high symmetry directions of the Brillouin zone; colors show the weight of the states at Bi (blue), Te (red), and Pb (green) atoms, respectively. Signs of  $\delta_i = \pm 1$  at the TRIM are shown also. (b) Calculated surface (solid line) and bulk continuum states (shaded) of  $\text{PbBi}_2\text{Te}_4$  along  $\bar{K}$ - $\bar{\Gamma}$ - $\bar{M}$  line. The inset shows the surface Dirac cones in the limited momentum space for  $\bar{\Gamma}$ - $\bar{M}$  and  $\bar{\Gamma}$ - $\bar{K}$  lines.

cal bulk and surface band structures of  $\text{PbBi}_2\text{Te}_4$ , which were obtained by *ab initio* calculations using the VASP code [32, 33] with optimized internal lattice parameters. In principle, three-dimensional materials with inversion symmetry are classified with four  $\mathbb{Z}_2$  topological invariants  $\nu_0; (\nu_1\nu_2\nu_3)$  which can be determined by a parity  $\xi_m(\Gamma_i)$  of occupied bands at eight time-reversal invariant momenta (TRIM)  $\Gamma_{i=(n_1, n_2, n_3)} = (n_1\mathbf{b}_1 + n_2\mathbf{b}_2 + n_3\mathbf{b}_3)/2$ , where  $\mathbf{b}_1, \mathbf{b}_2, \mathbf{b}_3$  are primitive reciprocal-lattice vectors, and  $n_j=0$ , or 1 [1, 2]. The  $\mathbb{Z}_2$  invariants are determined by the equations  $(-1)^{\nu_0} = \prod_{i=1}^8 \delta_i$  and  $(-1)^{\nu_k} =$

$\prod_{n_k=1; n_j \neq k=0,1} \delta_{i=(n_1, n_2, n_3)}$ , where  $\delta_i = \prod_{m=1}^N \xi_{2m}(\Gamma_i)$  [2]. For rhombohedral lattice of  $\text{PbBi}_2\text{Te}_4$  the TRIMs are  $\bar{\Gamma}$ ,  $\bar{Z}$ , and three equivalent L as well as F points, shown in Fig.1(b). Previous study confirmed that this compound is a strong topological insulator with the principal topological invariant  $\nu_0 = 1$  [27]. Here we have extended

the analysis for estimating the  $(\nu_1\nu_2\nu_3)$  invariants. Interestingly, the parity inversion of bulk bands occurs at the Z point for  $\text{PbBi}_2\text{Te}_4$  (Fig. 5(a)) that leads to  $\mathbb{Z}_2$  invariants 1; (111). This is in contrast to the case of binary  $\text{Bi}_2\text{X}_3$  (X=Se, Te) chalcogenides where the parity inversion takes place at the  $\bar{\Gamma}$  point with  $\mathbb{Z}_2$  invariant 1; (000) [3]. Note that  $\text{PbBi}_2\text{Te}_4$  is the first case among the experimentally established topological insulators with  $\mathbb{Z}_2$  invariant 1; (111) possessing a single Dirac cone surface state, which can be distinguished from  $\text{Bi}_{1-x}\text{Sb}_x$  alloy with the same  $\mathbb{Z}_2$  invariant [34] but with 5 or 3 pairs of surface states crossing the Fermi energy [7, 8]. In  $\text{Bi}_{1-x}\text{Sb}_x$  owing to nonzero invariants  $(\nu_1\nu_2\nu_3)$  the 1D topologically protected state can exist at dislocation core [35]. In the case of the layered crystal the bulk dislocations hardly can exist but other types of 1D TI states, like edge states in thin films or 1D states at step edges can be possible.

Finally we compare the experimental ARPES results with the theoretical band structures in Fig.5(b). The calculated band structure well reproduces the bulk conduction band minimum located at  $\bar{\Gamma}$  point at 200 meV above the Dirac point. Although the bulk valence band maximum energy is higher in theory than that in experiment, the theory well reproduces the location in  $\mathbf{k}$ -space, that is, it appears around  $1/3\bar{\Gamma}\bar{M}$  ( $k_{\parallel} \sim 0.3 \text{ \AA}^{-1}$ ). Anisotropic features along different symmetry lines can be recognized above 100 meV from the Dirac point as depicted in the inset. In addition, the parabolic surface state appears at  $\sim 280$  meV above the Dirac point in the conduction band gap, which is consistent with the present observation.

Our conclusion led by the present experiment is two fold: (i)  $\text{PbBi}_2\text{Te}_4$  is proved to be the three-dimensional topological insulator with the energy gap of 230 meV, accompanying a single Dirac cone at the  $\bar{\Gamma}$  point. (ii) The size of the Fermi surface contours are significantly large in the bulk energy gap region that provides the highest topological surface carrier density among the other 3D topological insulators. These novel findings pave an effective way for controlling the group velocity with sufficiently large spin current density by tuning the chemical potential in the topological quantum transport region.

We thank Shuichi Murakami for valuable comments. We also thank J. Jiang, H. Hayashi, T. Habuchi and H. Iwasawa for their technical support in the ARPES measurement at Hiroshima Synchrotron Radiation Center (HSRC). The ARPES measurement was performed with the approval of the Proposal Assessing Committee of HSRC (Proposal No.11-A-3, 11-A-4). The SPRING-8 experiments were carried out with the approval of the Japan Synchrotron Radiation Research Institute (JASRI) (Proposal No. 2010B0084, 2011A0084). This work was financially supported by KAKENHI (Grant No. 20340092, 23340105), Grant-in-Aid for Scientific Research (B) of JSPS. Calculations were performed on SKIF-Cyberia (Tomsk State University) and Arina

(UPV/EHU) supercomputers.

---

\* Electronic address: akiok@hiroshima-u.ac.jp

- [1] L. Fu, C.L. Kane, and E.J. Mele, Phys. Rev. Lett. **98**, 106803 (2007).
- [2] L. Fu, and C.L. Kane, Phys. Rev. B **76**, 045302 (2007).
- [3] M.Z. Hasan, and C.L. Kane, Rev. Mod. Phys. **82**, 3045 (2010).
- [4] X.L. Qi, and S.C. Zhang, Rev. Mod. Phys. **83**, 1057 (2011).
- [5] Q.K. Xue, Nat. Nanotechnol. **6**, 197 (2011).
- [6] F. Xiu, L. He, Y. Wang, L. Cheng, L.T. Chang, M. Lang, G. Huang, X. Kou, Y. Zhou, X. Jiang, Z. Chen, J. Zou, A. Shailos, and K.L. Wang, Nat. Nanotechnol. **6**, 216 (2011).
- [7] D. Hsieh, Y. Xia, L. Wray, D. Qian, A. Pal, J.H. Dil, J. Osterwalder, F. Meier, G. Bihlmayer, C.L. Kane, Y.S. Hor, R.J. Cava, and M.Z. Hasan, Science **323**, 919 (2008).
- [8] A. Nishide, A.A. Taskin, Y. Takeichi, T. Okuda, A. Kakizaki, T. Hirahara, K. Nakatsuji, F. Komori, Y. Ando, and I. Matsuda, Phys. Rev. B **81**, 041309 (2010).
- [9] Y.L. Chen, J.G. Analytis, J.-H. Chu, Z.K. Liu, S.-K. Mo, X.L. Qi, H.J. Zhang, D.H. Lu, X. Dai, Z. Fang, S.C. Zhang, I.R. Fisher, Z. Hussain, Z.-X. Shen, Science **325**, 178 (2009).
- [10] D. Hsieh, Y. Xia, D. Qian, L. Wray, F. Meier, J.H. Dil, J. Osterwalder, L. Patthey, A.V. Fedorov, H. Lin, A. Bansil, D. Grauer, Y.S. Hor, R.J. Cava, and M.Z. Hasan, Phys. Rev. Lett. **103**, 146401 (2009).
- [11] Y. Xia, D. Qian, D. Hsieh, L. Wray, A. Pal, H. Lin, A. Bansil, D. Grauer, Y.S. Hor, R.J. Cava and M.Z. Hasan, Nature Phys. **5**, 398 (2009).
- [12] K. Kuroda, M. Arita, K. Miyamoto, M. Ye, J. Jiang, A. Kimura, E.E. Krasovskii, E.V. Chulkov, H. Iwasawa, T. Okuda, K. Shimada, Y. Ueda, H. Namatame, and M. Taniguchi, Phys. Rev. Lett. **105**, 076802 (2010).
- [13] R.C. Hatch, M. Bianchi, D. Guan, S. Bao, J. Mi, B.B. Iversen, L. Nilsson, L. Hornekær, and P. Hofmann, Phys. Rev. B **83**, 241303(R) (2011).
- [14] J.G. Analytis, J.H. Chu, Y. Chen, F. Corredor, R.D. McDonald, Z.X. Shen, and I.R. Fisher, Phys. Rev. B **81**, 205407 (2010).
- [15] K. Eto, Z. Ren, A.A. Taskin, K. Segawa, and Y. Ando, Phys. Rev. B **81**, 195309 (2010).
- [16] N.P. Butch, K. Kirshenbaum, P. Syers, A.B. Sushkov, G.S. Jenkins, H.D. Drew, and J. Paglione, Phys. Rev. B **81**, 241301(R) (2010).
- [17] S. Kim, M. Ye, K. Kuroda, Y. Yamada, E.E. Krasovskii, E.V. Chulkov, K. Miyamoto, M. Nakatake, T. Okuda, Y. Ueda, K. Shimada, H. Namatame, M. Taniguchi, and A. Kimura, Phys. Rev. Lett. **107**, 056803 (2011).
- [18] S.V. Eremeev, Yu.M. Koroteev, and E.V. Chulkov, Pis'ma Zh. Eksp. Teor. Fiz. **91**, 664 (2010) [JETP Lett. **91**, 594 (2010)].
- [19] S.V. Eremeev, G. Bihlmayer, M. Vergniory, Yu.M. Koroteev, T.V. Menshchikova, J. Henk, A. Ernst, and E.V. Chulkov, Phys. Rev. B **83**, 205129 (2011).
- [20] K. Kuroda, M. Ye, A. Kimura, S.V. Eremeev, E.E. Krasovskii, E.V. Chulkov, Y. Ueda, K. Miyamoto, T. Okuda, K. Shimada, H. Namatame, and M. Taniguchi, Phys. Rev. Lett. **105**, 146801 (2010).
- [21] B. Yan *et al.*, Euro Phys. Lett. **90**, 37002 (2010).
- [22] H. Lin, R.S. Markiewicz, L.A. Wray, L. Fu, M.Z. Hasan, and A. Bansil, Phys. Rev. Lett. **105**, 036404 (2010).
- [23] T. Sato *et al.*, Phys. Rev. Lett. **105**, 136802 (2010).
- [24] Y.L. Chen *et al.*, Phys. Rev. Lett. **105**, 266401 (2010).
- [25] S.V. Eremeev, Yu.M. Koroteev, and E.V. Chulkov, Pis'ma Zh. Eksp. Teor. Fiz. **92**, 183 (2010) [JETP Lett. **92**, 161 (2010)].
- [26] H. Jin, J.H. Song, A.J. Freeman, and M.G. Kanatzidis, Phys. Rev. B **83**, 041202(R) (2011).
- [27] T.V. Menshchikova, S.V. Eremeev, Yu.M. Koroteev, V. M. Kuznetsov, and E.V. Chulkov, Pis'ma Zh. Eksp. Teor. Fiz. **93**, 18 (2010) [JETP Letters **93**, 15 (2011)].
- [28] L.E. Shelimova, O.G. Karpinskii, T.E. Svechnikova, E.S. Avilov, M.A. Kretova, and V.S. Zemskov, Neorg. Mater. **40**, 1440 (2004) [Inorg. Mater. **40**, 1264 (2004).]
- [29] T.B. Zhukova and A.I. Zaslavskii, Soviet Physics Crystallography **16**, 796 (1971).
- [30] I.I. Petrov and R. M. Imamov, Soviet Physics Crystallography **15**, 593 (1970).
- [31] O.G. Karpinskii, L.E. Shelimova, E.S. Avilov, M.A. Kretova, and V.S. Zemskov, Neorg. Mater. **38**, 24 (2002) [Inorg. Mater. **38**, 17 (2002).]
- [32] G. Kresse, J. Furthmüller, Comput. Mater. Sci. **6**, 15 (1996).
- [33] G. Kresse, D. Joubert, Phys. Rev. B **59**, 1758 (1999).
- [34] J.C.Y. Teo, L. Fu, and C.L. Kane, Phys. Rev. B **78**, 045426 (2008).
- [35] Y. Ran, Y. Zhang, and A. Vishwanath, Nat. Phys. **5**, 298 (2009).